ACS APPLIED MATERIALS & INTERFACES

Research Article

Cite This: ACS Appl. Mater. Interfaces 2018, 10, 5050−5060

www.acsami.org

Self-Assembled Layering of Magnetic Nanoparticles in a Ferrofluid on Silicon Surfaces

Katharina Theis-Bröhl,[*,†] Erika C. Vreeland,[‡,§] Andrew Gomez,[‡] Dale L. Huber,[‡] Apurve Saini,[∥] Max Wolff,[∥] Brian B. Maranville,[⊥] Erik Brok,[⊥,#,¶] Kathryn L. Krycka,[⊥] Joseph A. Dura,[⊥] and Julie A. Borchers[⊥]

[†]University of Applied Sciences, An der Karlstadt 8, 27568 Bremerhaven, Germany

[‡]Sandia National Laboratories, Albuquerque, New Mexico 87185, United States

[§]Imagion Biosystems LLC, Albuquerque, New Mexico 87106, United States

[∥]Division for Materials Physics, Uppsala University, 75120 Uppsala, Sweden

[⊥]NIST Center for Neutron Research, 100 Bureau Drive, Gaithersburg 20899-6102, United States

[#]Department of Materials Science and Engineering, University of Maryland, College Park, Maryland 20742, United States

Supporting Information

ABSTRACT: This article describes the three-dimensional self-assembly of monodisperse colloidal magnetite nanoparticles (NPs) from a dilute water-based ferrofluid onto a silicon surface and the dependence of the resultant magnetic structure on the applied field. The NPs assemble into close-packed layers on the surface followed by more loosely packed ones. The magnetic field-dependent magnetization of the individual NP layers depends on both the rotational freedom of the layer and the magnetization of the adjacent layers. For layers in which the NPs are more free to rotate, the easy axis of the NP can readily orient along the field direction. In more dense packing, free rotation of the NPs is hampered, and the NP ensembles likely build up quasi-domain states to minimize energy, which leads to lower magnetization in those layers. Detailed analysis of polarized neutron reflectometry data together with model calculations of the arrangement of the NPs within the layers and input from small-angle scattering measurements provide full characterization of the core/shell NP dimensions, degree of chaining, arrangement of the NPs within the different layers, and magnetization depth profile.

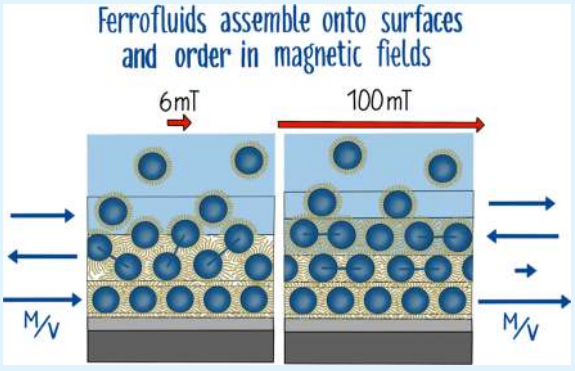

KEYWORDS: *magnetite nanoparticles, core/shell nanoparticles, ferrofluid, polarized neutron reflectometry, self-assembly, 3D self-ordering, quasidomains*

INTRODUCTION

Advances in the synthesis of well-defined nanoparticles (NPs) have opened up opportunities for their application in various fields.[1−5] Using the properties of small structures as individual objects is one important aspect of nanotechnology. There is, however, also a high interest in ensembles of NPs to use their collective behavior in functional devices. Ensembles of NPs can have properties that differ from those of individual particles as well as from those of the bulk.[6] Potential applications include the improvement of the mechanical properties of materials[7] or the introduction of new electronic,[8] magnetic,[9−11] photonic,[12] or optical functionalities.[8] Of particular interest are magnetite (Fe_3O_4) NPs developed and engineered for potential biomedical applications (e.g., superparamagnetic relaxometry (SPMR),[13−15] magnetic particle imaging,[16−18] and magnetic hyperthermia[19,20]) because of their low toxicity, strong response to magnetic fields, and superparamagnetic relaxation.

The key to well-ordered NP ensembles is self-assembly. Self-assembly is a low-cost method that provides controllable, simple mechanisms for the arrangement of the NPs into ordered structures, which can be achieved either through the direct interaction of the building blocks or by using a template or external field.[21−24] In the present work, we study the self-assembly of magnetite NPs in a ferrofluid (FF) adjacent to a silicon surface with an applied magnetic field. FFs are colloidal suspensions of magnetic NPs with typical sizes ranging from a few nanometers to several tens of nanometers. To prevent agglomeration, surfactants providing steric repulsion are attached to their surface. In solution, the NPs can form various heterogeneous structures such as linear chains, clusters, closed rings, and branched structures[25−27] depending on their

Received: October 4, 2017
Accepted: January 4, 2018
Published: January 4, 2018

DOI: 10.1021/acsami.7b14849
ACS Appl. Mater. Interfaces 2018, 10, 5050−5060

concentration. In the absence of a magnetic field, the observed netlike structures have been attributed to magnetic dipolar interactions.[28] The dipole interactions can be enhanced substantially if each NP is comprised of a single magnetic domain,[24,25,27,29−31] as in the case of our current study.[5] In addition, the magnetic response of a single-domain particle to a magnetic field differs substantially from that of a multidomain particle.[32] Instead of inducing domain wall displacement, the applied field must either rotate the entire magnetic moment within the NP or physically reorient the NP itself.[24] The balance among these complex magnetic forces and interactions thus plays an essential role in the bottom-up construction of nanoarchitectures, which are of high fundamental and practical importance.

Previously, we performed neutron reflectivity studies in which we observed a close-packed wetting layer of magnetite NPs on a silicon dioxide surface of a Si substrate.[33] The FF was highly concentrated (around 5 vol % Fe_3O_4), and the slightly nonspherical NPs with an average core diameter of 11 nm had a broad size distribution of around 30%. The particles were dissolved in water (i.e., a mixture of D_2O and H_2O) and dispersed with oleic acid. The oleic acid attached to the hydrophilic surface of the carefully cleaned silicon wafer. Under the influence of an in-plane magnetic field, the particles turned and oriented with their long axis along the field direction. Under shear, the particles showed a static wetting at the surface and a depletion layer between the static layer and the moving FF. The shape anisotropy and size polydispersity in this NP system clearly have a significant effect on the self-assembly process.

The aims of the present study are to determine if the substrate wetting can be initiated in a dilute, 0.15%, FF system with monodispersed, spherical particles comprised of a single magnetic domain and if the self-assembly process can then be systematically controlled by application of a small magnetic field. An important question to answer is whether the particles would fully wet the surface of the specially prepared template in a well-defined, densely packed configuration despite the reduced concentration of the particles in solution. In addition, the aim is to determine if an applied field can significantly alter the resultant physical structure in the absence of NP structural inhomogeneities. With these goals, we first performed small angle neutron scattering (SANS) measurements to characterize the structural and magnetic order of the individual particles that make up the FF. Subsequently, polarized neutron reflectivity (PNR) studies of a FF in contact with a silicon surface were used to ascertain the depth-dependent profiles of the nuclear and magnetic structures in the direction perpendicular to the silicon surface. Determination of the structural configuration relied upon a detailed comparison of the experimentally determined scattering length density (SLD) values to those derived from model calculations assuming a certain fractional packing in a particular layer. Furthermore, using polarized neutrons, we were also able to isolate the magnetization depth profile and probe the unexpected changes in both the structural and magnetic order that were induced by the applied field.

The FF used for this investigation was prepared by Imagion Biosystems.[5] The well-defined monocrystalline and spherical particles with a core diameter of 25 nm are designed for use in SPMR, magnetic hyperthermia, and other biomedical applications. SPMR requires tight control of the particle size because it affects the performance of the magnetite NPs very sensitively in vitro. Figure 1a shows a representative image of the particles.

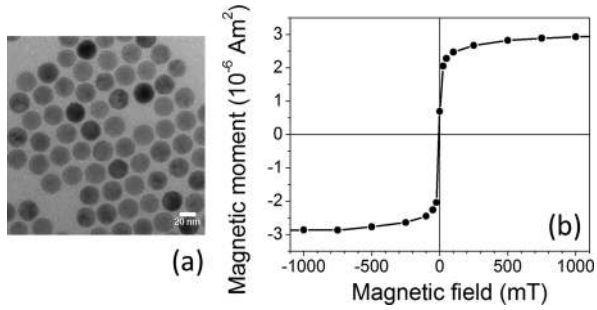

Figure 1. Representative TEM image of 25 nm particles used in the present study (a) and magnetization curve of the magnetite NPs, as measured with SQUID magnetometry (b).

The magnetite particle cores are coated with a monolayer of oleic acid and a monolayer of an amphiphilic polymer with carboxylic acid. This kind of coating makes them very stable in water and also provides anchors for attaching the NPs to a functionalized surface. From our SANS data, we determined the NPs to have a core diameter of 25.3 nm with a narrow size distribution of 10%, as described below. The NPs were dissolved in a water mixture with 85% D_2O and 15% H_2O, which was selected to decrease the incoherent background scattering and to increase the contrast for the neutron scattering experiments. The concentration of the NPs in the FF was chosen to be low (around 0.15 vol % Fe_3O_4), corresponding to approximately 8 mg/mL of Fe_3O_4 to investigate the mechanisms for building densely packed structures from a very dilute system.

The NP ensemble shows superparamagnetism at room temperature. The magnetization curve is shown in Figure 1b. According to superconducting quantum interference device (SQUID) measurements, the sample is saturated in a field of approximately 3 T and has a saturation magnetization of 379 emu/cm^3, relative to the Fe_3O_4 bulk magnetization of 524 emu/cm^3.[34−36,a]

To bind the particles to the template for the neutron reflectivity measurements, a (3-aminopropyl)triethoxysilane (APTES) layer was deposited onto a silicon wafer that was used in the wet cell. The interaction of the carboxylic groups of the NPs with the silane layer is visualized in Figure 2.

RESULTS AND DISCUSSION

SANS Results. Information about the internal NP structure and their collective interactions (e.g., chain or cluster formation) in a FF was obtained from SANS investigations.

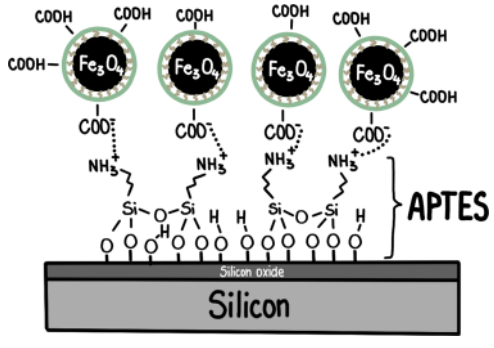

Figure 2. Schematic drawing of the amine bond between the silane group of the APTES layer and the carboxylic group of the NP ligands.

DOI: 10.1021/acsami.7b14849
ACS Appl. Mater. Interfaces 2018, 10, 5050−5060

SANS data for the FF in D_2O used in this investigation are shown in Figure 3. Model fits reveal that the particles have a

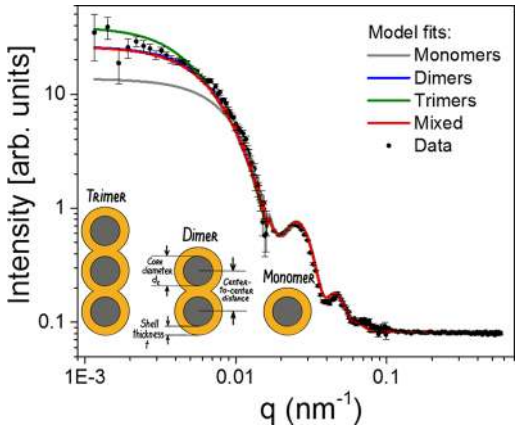

Figure 3. SANS data taken from the FF used in the present study and fits of the data to several models.

core diameter of 25.3 nm and that water penetrates into the shell, which leads to an SLD value that is higher than expected for the bulk shell material (see the Supporting Information for details). This phenomenon can be explained by the hydrophilicity of the heads of the oleic acid ligands, which are attached to the NP. The heads attract water that penetrates all the way through the NP shell, giving a total shell thickness of 6.6 nm.

Polarization analyzed SANS (PASANS) experiments performed on related NPs in a near-zero field[37] reveal that the magnetic core orders as a single domain with a diameter of (23.6 ± 0.4) nm[b], relative to a structural core size of (25.0 ± 0.4) nm, consistent with a 0.7 nm surface layer with a reduced or disordered magnetization. Furthermore, the NPs form only short chains in the FF, and the chain lengths differ slightly from batch to batch. Specifically, the NPs form a combination of trimers, dimers, and monomers in water. The best fit (red line) to the SANS data in Figure 3 suggests that the FF used in our investigation is predominantly composed of dimers (around 81% in volume) with some monomers (around 10% in volume) and some trimers (around 9%). For comparison, model fits with just monomers (gray line), dimers (blue line), or trimers (green line) are shown in Figure 3 as well. The parameters from the best fit for the "mixed" model are summarized in Table 1.

Subtraction of the core diameter from the center-to-center distance in the dimers and trimers (34.0 nm from SANS fits) indicates that each shell is compressed to t = 4.4 nm between the particles. This value is in excellent agreement with the results obtained from PNR fits for the core/shell particle diameter d_{c+s} (described below) and is about 2 nm smaller than the average thickness of the shell (6.6 nm) determined directly from the SANS fits (Table 1). We thus conclude that the ligands between the cores in the dimers and trimers are somewhat compressed or displaced compared to the unconfined shell.

Neutron Reflectometry (NR) Results. NR was used to characterize the NPs' self-assembly onto a silicon/APTES template. Specular NR gives the depth profile of the SLD, averaged in the plane of the sample over the coherence volume of the neutron beam, which is on the order of a micrometer in the in-plane x direction[38−41] (the scattering geometry is shown in Figure S1 in the Supporting Information). We used unpolarized and then polarized neutrons to determine both the nuclear and magnetic depth profiles. Our measurements with unpolarized neutrons in zero field and 100 mT (shown in the Supporting Information) provided definitive proof of NP self-assembly onto the silicon surface and subsequently guided the fits to the PNR data. The PNR measurements were performed with a slightly different instrumental setup in a high magnetic field of 100 mT and then in a lower magnetic field of 6 mT. We focus here on the results of the PNR measurements because the fits are highly sensitive to both the nuclear depth profile Nb(z) and the magnetic depth profile Np(z). The FF was not expected to have exactly the same structural configuration in low fields (0 and 6 mT) because changing the magnetic field could possibly move the particles. From the fits to PNR data, we found that the agreement between Nb for the two field configurations was fairly good. We did, however, obtain slight differences in the nuclear SLDs of the layers for the measurements with unpolarized and polarized neutrons.

Figure 4a shows the PNR data with $R{\cdot}q_z^4$ plotted as a function of q_z and the error bars corresponding to ±1 standard deviation. The splitting between the (++) and (−−) reflectivity cross-sections, which originates from the projection of the magnetization parallel to the applied field (for details see Methods), is highlighted in the plots of the spin asymmetry (SA) [Figure 4b,c]. The best fits to the data with χ^2 = 8.0 and 4.9 are shown as solid lines in Figure 4. The resulting Nb(z) and Np(z) SLD profiles are plotted in Figure 5.

The construction and interpretation of these model profiles are described below. The SLDs of several key components of the NP system (see the Supporting Information for details) were calculated using the SLD of the FF, that is, $Nb_{FF} = 5.27 \times 10^{-4}$ nm^{-2} (obtained from the unpolarized fits), the known concentration of magnetite in the solution (0.15 vol %), the core diameter of 25.3 nm, and the two cases of compressed and stretched core/shell diameters of 34.0 and 38.5 nm, respectively. For comparison, the bulk SLD values of these FF components are given in Table S2 in the Supporting

Table 1. Results of Fits to the SANS Data Using a Model Containing Monomers, Dimers, and Trimers[c]

	d_c rsp. t [nm]	Nb [10^{-4} nm^{-2}]	Np [10^{-4} nm^{-2}]	poly-disp. (%)	volume fraction (%)	volume fraction (%)	center-to-center distance [nm]
core	25.3 ± 0.3	6.91 (fixed)	1.50 ± 0.20	10	0.06		
shell	6.6 ± 0.4	4.28 ± 0.03					
solvent		6.35 ± 0.70					
monomers						10	
dimers						81	34.0 ± 0.3
trimers						9	

[c]Given are the core diameter d_c, shell thickness t, nuclear SLD (Nb) of the core, shell, and solvent (D_2O), and magnetic SLD (Np), volume fraction, and dispersity of the core. The volume fractions of the monomers, dimers, and trimers are provided, as well as the dimer center-to-center distance.

DOI: 10.1021/acsami.7b14849
ACS Appl. Mater. Interfaces 2018, 10, 5050−5060

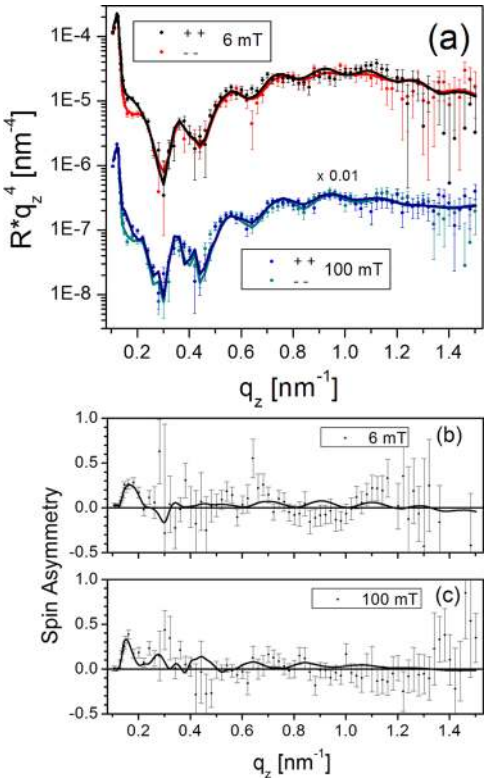

Figure 4. Top: PNR data taken when applying magnetic fields of 6 and 100 mT (a). Shown are plots of $R{\cdot}q_z^4$ as a function of q_z. The solid lines represent fits to the data. The data and fits of the measurements in a field of 100 mT were shifted with respect to the data and fits in 6 mT by a factor of 0.01 for better visibility. Bottom: SAs at 6 (b) and 100 mT (c).

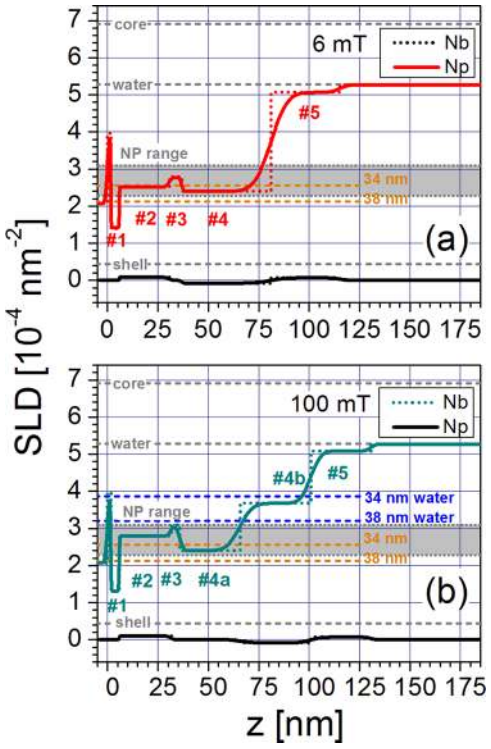

Figure 5. Profiles of nuclear Nb(z) and magnetic Np(z) SLDs plotted as a function of distance z from the Si(100) surface determined from the results of the fits to the PNR data taken at 6 (a) and 100 mT (b) and shown in Figure 4. For comparison, SLD values for the magnetite core, water, and shell material are also included as gray dashed lines. Model calculations for the NP SLD find different values for compressed or stretched ligands in the shell. The SLD range between the compressed and stretched ligand model for isolated NPs is shown as a gray area. Furthermore, model SLD values for a close-packed layer of truncated particles with shell material in the intershell gaps (orange dashed lines) and with water in the intershell gaps (blue dashed lines) are given for core/shell NP diameters of 34 and 38 nm, respectively.

Information and are included as gray lines in the SLD profile plots in Figure 5. Furthermore, the calculated SLD values for different arrangements of the particles in truncated particle single layers or in a double layer (discussed below) are included in blue and orange (see SLD values in Table S2).

Because unpolarized data are more straightforward to fit, we used these results to predefine parameters for our fits to the polarized data, as described in the Methods section. Specifically, we determined the number of uniform slabs in the model from the unpolarized data, and we obtained preliminary information about the nuclear SLD and thickness of these slabs.

The bottom slab in the stack is native SiO_2 (on the Si wafer) with a thickness of 1.8 nm and an SLD of 3.97×10^{-4} nm^{-2}, as determined from a fit to the reflectivity data (not shown) obtained with only $D_2O/SiO_2/Si$ (and without NPs). The parameters of this slab were fixed in subsequent fits to the FF data (Figure 4). For both magnetic fields, we find that a layer of NPs wets the silicon surface, producing three distinct slabs in the SLD depth profiles that were fit to the data. The first slab above the native oxide, #1 in the model, was determined to consist mainly of shell material (which included the shells attached to the NPs and in the interstitial regions between the NPs), excess additive material (which was included in the FF to produce the shells around the magnetic particles), and possibly some water. The APTES layer is too thin and has too little contrast with the shell material to be resolved by neutron reflectivity and is also included in this slab. The next slab of the stack (#2) contains the cores of the particle wetting layer, shell material between the cores, as well as some D_2O/H_2O. The ligand shell on the opposite side of these particles forms the next distinct slab (#3).

Further layering was found on top of the first NP wetting layer although distinct slabs attributable to just shells are not expected beyond slab #3 because of layer roughness. Thus, slab #4 in 6 mT (or slabs #4a and #4b in 100 mT) is an additional region of particles containing both core and shell material as well as some water. The presence of additional NP layers in between the wetting layer (slabs #1–#3) and the bulk FF is a new observation that contrasts with results from our previous studies.[33] Not only does this region expand in thickness from 44.4 to 65.0 nm with increasing field but it also evolves from a single layer into two distinct layers with different SLDs (slabs #4a and #4b) at 100 mT. The specifics of the dependence of this structure on the field will be discussed in more detail below. Finally, slab #5 is a magnetized particle layer that forms a broad interface with the adjacent bulk FF, which does not carry a magnetic moment itself. In addition, the layer model includes the SLD of the bulk FF on top of the stack, together with its roughness.

To interpret the SLD profiles in Figure 5 in terms of the arrangement of the particles within the individual slabs according to Figure 6, we modeled an idealized layer of close-packed particles. In this hexagonal model (see Figure S7 in the Supporting Information), the core/shell particles build a

DOI: 10.1021/acsami.7b14849
ACS Appl. Mater. Interfaces 2018, 10, 5050–5060

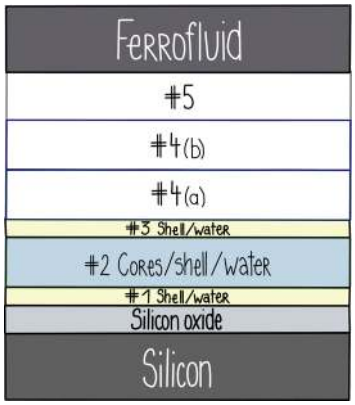

Figure 6. Sketch of the stack assumed for the fits of the neutron reflectivity data.

single sheet of particles as exemplified by slab #2, which includes only the center region truncated at the planes tangent to the cores.

Field Dependence of the NP Layer Structure. Conclusions regarding the self-assembly process for the FF system onto the silicon template are drawn from the nuclear depth profile obtained from PNR (Figure 5 and Table 2) as compared to the SLD model calculations (Tables S2 and S3 in the Supporting Information). The changes in the composition and structure of each of the primary layers as a function of the applied magnetic field are described below.

The wetting layer on the surface of silicon can be described as a single particle monolayer comprised of distinct slabs #1−3 [Figures 6 and 7a]. Slab #1 mainly contains ligand shell material. Its thickness of about 4 nm agrees well with the shell thickness between the Fe_3O_4 particles in the dimers corresponding to one of their two shells. This single shell thickness is smaller than the average shell thickness of 6.6 nm, which is measured predominantly in directions other than the dimer axis (Table 1). The ligands adjacent to the silicon surface thus appear to be compressed to the same length as that of the ligands separating the dimers. Assuming that slab #1 contains only shell material and water (consistent with SANS measurements), the water content can be determined from the fitted SLD value ($Nb_{\#1} \approx 1.4 \times 10^{-4}$ nm^{-2}) to be about 20% by volume. This low value suggests that the spaces between the spherical shell caps are partially filled with excess ligand material that is either attached to the APTES layer on the silicon surface or originates from the deformations of the shell at the surface.

Slab #2 is the most important part of the wetting layer because it contains the ordered magnetic cores. In both low and high magnetic fields, its thickness (around 25 nm) is in excellent agreement with the core diameter d_c measured by various methods. Its roughness was found to be below 1 nm, indicating that this layer is well-defined and planar. Because the cores are surrounded by a ligand shell, this layer also contains shell material and possibly some water in the spaces between the core/shell particles. Comparing the nuclear SLD value from the fit of the 6 mT data $Nb_{\#2} = 2.51 \times 10^{-4}$ nm^{-2} to the SLD model calculations for a close-packed layer of particles (Table S3 in the Supporting Information), the slab is best described by a close-packed layer with the spaces between the particles filled by ligands [Figure 7a]. The shells surrounding each core are either compressed or overlapped, with the material from the deformed shells filling most of the interparticle gaps. The model calculations (orange dashed line labeled "34 nm" in Figure 5) suggest an average center-to-center distance of the particles of 34 nm with no water being present in this layer and volume fractions of 33% Fe_3O_4 and 67% ligand material. This center-to-center distance agrees well with the compressed core/shell diameter of 34.0 nm (see above). It is more likely, however, that slab #2 contains water as well because the adjacent slabs #1 and #3 (see below) include some water. As water has a high SLD, this can only be compensated by a greater amount of ligand material within this layer if the average center-to-center distance is a bit higher than 34 nm. At 100 mT, the SLD of slab #2 increases slightly, further supporting this increased water content. Assuming that the stretched core/shell diameter is 38.5 nm instead, the water content is approximately 9% by volume in slab #2, which corresponds to a volume fraction of 25% Fe_3O_4 and 66% ligand material. From these model calculations, it cannot be determined if the particles in the wetting layer are single NPs, dimers, or trimers. If dimers and/or trimers self-assemble in this layer, they obviously orient with their long axis parallel to the silicon surface.

Similar to slab #1, slab #3 consists of ligand shell material. Its thickness is slightly larger than that of slab #1, and its fitted nuclear SLD ($Nb_{\#3} \approx 2.8 \times 10^{-4}$ nm^{-2} is higher than the SLDs for slabs #1 and #2, suggesting that the water content is larger. Assuming that this layer does not contain any magnetite, the volume fraction of water is calculated to be approximately 50%. Though the nuclear SLD effectively does not change with the field, the layer thickness was found to be slightly smaller in a field of 100 mT (Table 2). With the exception of this slight variation in the SLD of slab #2 and in the slab #3 thickness, the entire particle wetting layer (slabs #1−#3) is stable and not influenced by the magnetic field. We thus conclude that the

Table 2. Slab Thickness, Roughness, and Nuclear SLD Values Obtained from Fits to the PNR Data Taken in Magnetic Fields of H = 6 mT and H = 100 mT

	H = 6 mT, χ^2 = 8.0				H = 100 mT, χ^2 = 4.9		
layer	thickness t [nm]	roughness Δt [nm]	nuclear SLD Nb [10^{-4} nm^{-2}]	layer	thickness t [nm]	roughness Δt [nm]	nuclear SLD Nb [10^{-4} nm^{-2}]
SiO_2	1.8	1.0	3.97	SiO_2	1.8	1.0	3.97
#1	4.1 ± 0.1	0.2 ± 0.1	1.42 ± 0.04	#1	4.1 ± 0.1	0.2 ± 0.1	1.31 ± 0.04
#2	24.7 ± 0.4	0.1 ± 0.1	2.51 ± 0.06	#2	25.8 ± 0.5	0.3 ± 0.1	2.80 ± 0.05
#3	6.1 ± 0.5	1.3 ± 0.5	2.77 ± 0.07	#3	4.2 ± 0.5	1.4 ± 0.6	3.09 ± 0.07
#4	44.4 ± 0.8	0.7 ± 0.5	2.40 ± 0.02	#4a	29.8 ± 2.1	1.5 ± 0.3	2.40 ± 0.01
				#4b	35.2 ± 0.7	5.1 ± 0.6	3.68 ± 0.04
#5	34.1 ± 0.9	6.5 ± 0.1	5.07 ± 0.02	#5	29.9 ± 1.5	4.0 ± 0.2	5.09 ± 0.04
FF		3.5 ± 1.1	5.27	FF		1.9 ± 0.5	5.27

DOI: 10.1021/acsami.7b14849
ACS Appl. Mater. Interfaces 2018, 10, 5050−5060

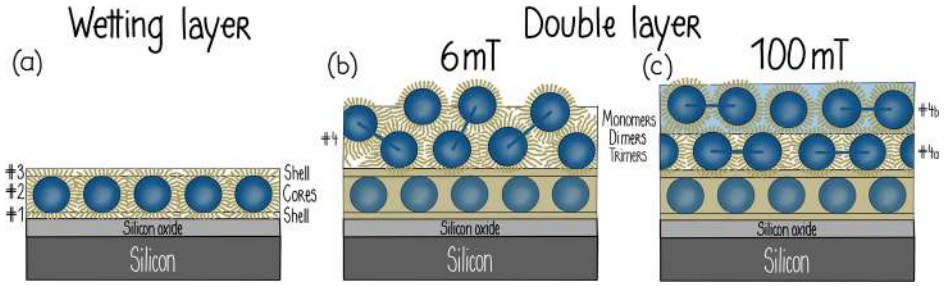

Figure 7. Schematic drawing of NP-ordering determined from the results of SANS and PNR. (a) Wetting layer, (b) double layer on top of the wetting layer in a magnetic field of 6 mT, and (c) double layer on top of the wetting layer in a magnetic field of 100 mT.

amine bond between the silane group of the APTES layer and the carboxylic groups of the shell tightly hold the densely packed layer of NPs onto the silicon surface (Figure 2) despite their low concentration in the FF.

The SLD profiles in Figure 5 show that additional particle layers assemble on top of the wetting layer (slabs #1–#3), and they change in response to different magnetic fields. Specifically, the fitted nuclear SLD for the slab adjacent to the wetting layer [#4 in Figure 5a and #4a in Figure 5b with $Nb_{\#4}$ (6 mT) ≈ $Nb_{\#4a}$ (100 mT) = 2.4 × 10^{-4} nm^{-2}] is independent of the magnetic field but has a slightly lower SLD than that of slab #2. This slab appears to be nearly completely close-packed with a water content similar to slab #2. In contrast to slab #2, the SLD of slab #4 is slightly smaller than that calculated for a close-packed structure with a compressed shell and shell material in the interstitial spaces (Table S3 in the Supporting Information). Instead, the SLD value tends toward that expected for an unconfined shell (orange dashed line labeled "38 nm" in Figure 5). Alternately, the lower SLD for slab #4 relative to that of slab #2 could originate from local disorder. Slab #4 might include shell material from above and below the plane of cores that, in the case of slab #2, is relegated to slabs #1 and #3 (Table S3 in the Supporting Information).

In 6 mT, this disorder is supported by the fact that the thickness of slab #4 was found to be about 44.4 nm (Table 2), which is significantly greater than the particle core diameter. Correspondingly, while the roughness of the interface between slab #2 and #3 is small, the roughness is much larger between slab #4 and slab #5, which has a SLD approaching the bulk FF value. We conclude that slab #4 consists of a mixture of monomers, dimers, and trimers that self-assemble on top of slab #3 to complete a monolayer plane. Some of the dimers and trimers are oriented parallel to the sample surface but others are oriented at various angles with respect to the silicon surface [Figure 7b], giving rise to enhanced interfacial roughness and a layer thickness that is somewhat smaller than that expected for a close-packed double layer of NPs.

In contrast, the thickness of slab #4a in 100 mT decreased to 29.8 nm (Table 2), which corresponds to about the particle diameter. From this, it can be inferred that in the higher magnetic field, the dimers rotate into the field direction and separate into two distinct slabs, #4a and #4b [Figure 7c]. In this case, the SLD and thickness of slab #4a are again consistent with expectations for a close-packed particle layer.

Slab #4b has a thickness of 35.2 nm, which is larger than that of slab #4a but in good agreement with the core/shell diameter of d_{c+s} = 34 nm determined from SANS (Table 1). The higher value of the fitted SLD ($Nb_{\#5}$ = 3.68 × 10^{-4} nm^{-2}) is roughly half way between the SLDs of slab #4a and the bulk FF, indicating that this slab consists of a monolayer of particles with water in both the interstitial gaps and the particle vacancies.

Finally, in both fields, slab #5 (Figures 5 and 6) has a nuclear SLD that does not deviate much from that of the adjacent bulk FF. Slab #5 is therefore not ordered into a dense layer, but rather has a NP concentration that is slightly higher than that of the bulk FF. This rough slab is magnetized, however, in contrast to the bulk FF, which does not carry a detectable net magnetic moment itself.

Magnetic Characteristics of the NP Layers. The layered structure clearly is altered by the application of a field, which presumably reorients the magnetic dipoles of the dimers and trimers via the Zeeman interaction. Our investigation revealed that the changes in the structure of the self-assembled layers are accompanied by variations in the magnetization of the NP layers, as anticipated. The variations in the magnetization are evidenced by the field-dependent features in the low q_z SA. Specifically, the peaklike feature below q_z = 0.2 nm^{-1} in the SA for 100 mT [Figure 4c] has a higher amplitude and is more narrow than the same feature in the SA for 6 mT [Figure 4b]. From fits to the PNR data (Figure 4), we obtained magnetic SLD profiles Np(z) in 6 and 100 mT, which are plotted in Figure 5 (in units 10^{-4} nm^{-2} = 10^{-6} $Å^{-2}$).

The magnetic component of the SLD Np is directly proportional to the sample volume magnetization with M/V = [1.47 × 10^{-7}/(16π) emu/cm^3·nm^2] × Np and is plotted in Figure 8. The values of M/V for the different slabs are also given in Table 3. Additionally the magnetizations $\int_{\#i} M/V\, dz$ integrated along depth z for the particular slabs #i are given. To calculate the magnetic moment per unit volume of Fe_3O_4, we used the nuclear SLD from our fits to the data (see Table 2) to determine the volume fraction of Fe_3O_4 for each slab.

In slabs #5 for 6 mT and #4b and #5 for 100 mT, the intershell gaps are filled with water, and the determination of the volume fraction of magnetite is not as straightforward. Therefore, we used the model SLD for a hard sphere NP with a core diameter of d_c = 25.3 nm and a core/shell diameter of d_{c+s} = 34.0 nm. By fixing the ratio of the core-to-shell material in this way, the volume fraction of all materials including water can be determined from the nuclear SLD values in Table 2. Using the sample volume magnetization M/V of the different slabs and the volume fractions of Fe_3O_4, we determined the volume magnetization M/V with respect to Fe_3O_4, as shown in Table 3. We give these values in emu/cm^3 and also relate them to the bulk saturation magnetization of magnetite of 524 emu/cm^3.

For the discussion of the magnetic behavior, we treat the NPs as single domain[5] because PASANS measurements[37] indicate that their core magnetization is uniform in low fields with only a thin layer of disordered surface spins. In addition,

DOI: 10.1021/acsami.7b14849
ACS Appl. Mater. Interfaces 2018, 10, 5050–5060

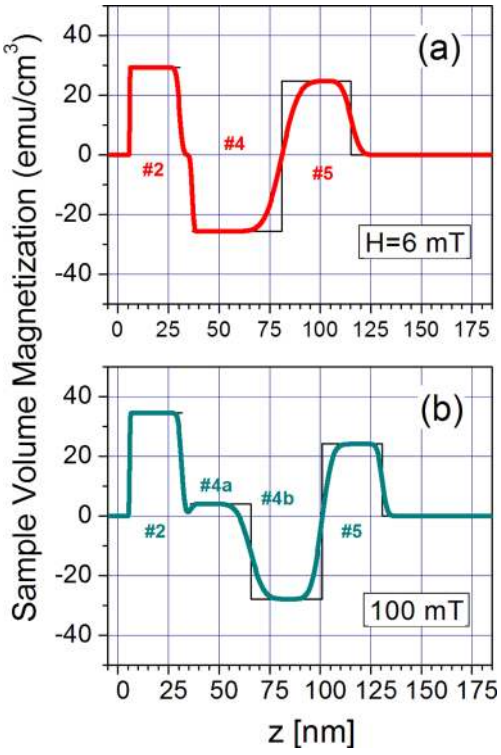

Figure 8. Profiles of sample volume magnetization M/V plotted as a function of distance z from the Si(100) surface determined from the results of the fitting routines applied to the PNR data shown in Figure 4 and recalculated from the magnetic SLDs Np for the measurement at 6 (a) and 100 mT (b). The volume used for the calculation is the unit volume of the material of the corresponding slab in our model (see above).

the energy of forming a domain wall is too high in these small particles within the range of fields applied here. Consequently, the remagnetization process under the influence of a magnetic field occurs through rotation of the net moment, rather than through domain wall motion within the NP. The energy barrier for magnetization rotation can be very high, as it is the integral of the magnetic anisotropy energy throughout the whole NP.[24] For sufficiently small particles, this energy can be on the order of the thermal energy, making the magnetization of individual NPs thermally unstable. The whole magnetization of the particle thus might flip via a process known as Néel relaxation.[42] In a liquid suspension, however, each NP is able to physically rotate by Brownian motion, which occurs on a much faster timescale.[43] The difference in the two timescales is actually key for the application of magnetic relaxometry for which these NPs are designed.[15]

Because of the large magnetic dipole interactions for these single-domain NPs, larger structures, such as dimers and trimers, self-assemble in the FF without the application of an external field.[24] As a consequence of the NPs' interaction with each other and with the APTES surface, the layers in the present FF system consist of NPs with a varying ease of rotation. Therefore, the magnetization process may differ from layer to layer because either Brownian motion or Néel relaxation may dominate.

Slab #5, which is close to the bulk FF, consists of only a small volume fraction of NPs, which do not interact with each other and are the most free to rotate their easy axes into the field direction. As can be seen from Table 3, our measurements support this assumption and reveal that this particular layer carries the highest magnetic moment in the stack: (114 ± 64)% of the magnetite saturation magnetization (which is 524 emu/cm^3) in low field and (125 ± 81)% in high field. (These relatively large uncertainties are due to the combination of uncertainties from two measured quantities, the fitted Nb and Np SLDs from Table 2. In addition, the propagated error associated with the NP SLD of (3.15 ± 0.6) 10^{-4} nm^{-2} from Table S2 in the Supporting Information assumes considerable uncertainty in the ligand shell and gap material SLDs.) Because the process of free rotation does not require as much energy as the Néel relaxation process, the magnetization changes within this loosely packed layer presumably occur rapidly and trigger the reorientation process of the magnetization of the remaining layers in the stack.

The magnetization of the layer adjacent to slab #5 then aligns antiparallel to it due to dipolar interactions. In the high-field case, the NPs in this adjacent layer (slab #4b) occupy a partial monolayer with higher water content than the more compact layers (slabs #4a and #2) closer to the Si surface and are thus more free to rotate to maintain antiparallel alignment with the magnetization of slab #5. The next particle layer, slab #4a in the high field, is located between this layer (slab #4b), which has its magnetization oriented antiparallel to the field, and the wetting layer, which has its magnetization aligned parallel to the field.

Table 3. Magnetic Parameters as Derived from the Fits to the PNR Data Taken in Fields of H = 6 mT and H = 100 mT[d]

slab	thickness t [nm]	magnetic SLD Np [10^{-4} nm^{-2}]	sample volume magn. M/V [emu/cm^3]	integrated magn. $\int_{\#i} M/V\,dz$ [10^{-7} emu/cm^2]	volume fraction Fe_3O_4 $V_{Fe3O4}/V_{\#i}$	volume magn. Fe_3O_4 [emu/cm^3]	rel. vol. magn. Fe_3O_4 [%]
			H = 6 mT				
#2	24.7 ± 0.4	0.09 ± 0.02	29 ± 8	726	0.31 ± 0.07	93 ± 34	18 ± 6
#4	44.4 ± 0.8	−0.07 ± 0.03	−26 ± 10	−1007	0.30 ± 0.07	−86 ± 40	−16 ± 8
#5	34.1 ± 1.0	0.07 ± 0.01	25 ± 2	718	0.04 ± 0.02	599 ± 336	114 ± 64
sum				437			
			H = 100 mT				
#2	25.8 ± 0.5	0.10 ± 0.011	35 ± 3	893	0.36 ± 0.08	96 ± 9	18 ± 2
#4a	29.8 ± 2.1	0.01 ± 0.01	4 ± 3	87	0.30 ± 0.07	14 ± 11	3 ± 2
#4b	35.2 ± 0.7	−0.08 ± 0.05	−27 ± 15	−768	0.31 ± 0.09	−90 ± 50	−17 ± 10
#5	29.9 ± 1.5	0.07 ± 0.01	24 ± 4	638	0.04 ± 0.02	654 ± 425	125 ± 81
sum				851			

[d]In addition to the magnetic SLDs (Np), the volume magnetization M/V, the integrated magnetization over the particular slab, the volume fraction of Fe_3O_4, the volume magnetization of Fe_3O_4, and the relative volume magnetization of Fe_3O_4 with respect to the bulk saturation magnetization of magnetite of 524 emu/cm^3 are given. Notice, only slabs which carry a magnetic moment are considered.

DOI: 10.1021/acsami.7b14849
ACS Appl. Mater. Interfaces 2018, 10, 5050−5060

Therefore, slab #4a (which has a higher ligand content than slab #4b) experiences high frustration that results in a low net magnetization. This layer consists of NPs that are mostly dimers oriented parallel to the silicon surface. Because of dipolar coupling, the NPs may order in a quasi-domain structure (shown schematically in Figure 9), as was suggested in the study by Mishra et al.[44] for spin-coated magnetic NP layers.

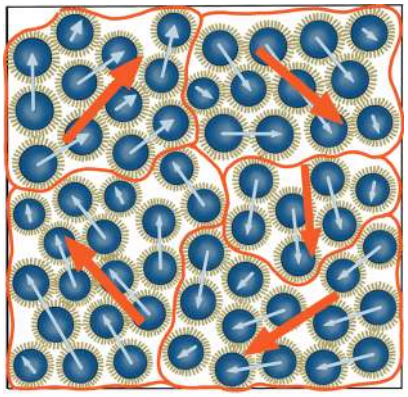

Figure 9. Sketch of a possible magnetic moment distribution within a NP layer when the NPs experience a quasi-domain configuration. The solid orange outlines represent the domain walls.

In contrast, there is only one magnetically monolithic layer between the outermost "dilute" layer and the wetting layer in the low-field case. As this layer (slab #4) can be antiparallel to both the adjacent layers, it does not experience the magnetic frustration apparent in the high-field case, and its magnetization is somewhat higher than that of slab #4a.

The magnetic NP cores in slab #2 of the wetting layer are bound via APTES to the Si surface and are assembled into a close-packed configuration. Therefore, they are probably not able to rotate easily under the influence of a magnetic field, and the magnetization itself needs to rotate instead. For both magnetic field cases, we observe that the magnetization of the wetting layer is oriented along the magnetic field direction. However, the relative volume magnetization of Fe_3O_4 in slab #2 is much less compared to that of slab #5 with unbound NPs (18% in low field and high field as stated in Table 3). Therefore, it can be assumed that a quasi-domain structure similar to that proposed for slab #4a in the high field (see sketch in Figure 9) may occur in the wetting layer as well. However, incomplete flux line closure in the wetting layer leads to a higher net magnetization than that of slab #4a. The magnetization in slab #4 in the low-field case has a magnitude that is similar to that of slab #2, but antiparallel. This layer is also close-packed as was concluded from the low nuclear SLD. Therefore, a similar quasi-domain state (Figure 9) can be assumed for slab #4.

It is interesting to note that the different mechanisms by which each layer magnetization is manipulated by the magnetic field are clearly revealed by PNR. Specifically, the particles in the loosely attached layers (such as slab #5) can rotate freely in order to orient their easy axes along the field direction, whereas the NPs in the bound layers (such as slab #2) are immobile with a lower net magnetization resulting from quasi-domain formation (Figure 9).

CONCLUSIONS

In summary, we observed three-dimensional (3D) self-assembly of spherical and monodisperse magnetite NPs from a dilute FF (concentration far below 1 vol %) onto a treated silicon surface via NR. The concentration of the NP cores in these structures can be up to 200 times higher than that in the dilute FF. Following the formation of a close-packed wetting layer, the NPs assemble into additional particle layers, including another close-packed layer and more loosely packed layers, with thicknesses and SLDs that depend on the magnetic field. Because of chain formation in the FF (predominantly dimers), the region close to the wetting layer consists of a double layer at low field, which splits into two clearly distinguishable particle layers under the influence of a high in-plane field. In both field cases (6 and 100 mT), the particles adjacent to the wetting layer are close-packed as in the wetting layer but with a slightly higher interparticle distance. Almost no water is present in the close-packed regions, and the interparticle gaps are filled with shell material. With increasing distance from the silicon surface, water can penetrate into the interparticle gaps.

It is notable that the very dilute, loose particle layer that forms between the free FF and the 3D self-assembled particle structure plays a key role in the magnetic behavior of the stack. Specifically, the magnetization orientation of the entire stack is triggered by this loose particle layer, which has a low volume concentration that nearly matches that of the free FF. As the particles in this layer do not strongly interact with the substrate or other particles, they are free to rotate into the field direction and thus have the highest net magnetization in the stack. In the other layers, the particles are bound more tightly because of different packing configurations and/or interstitial material composition. Therefore, the particles in these bound layers are less mobile and their magnetization cannot be changed as readily by rotation of the particles. The competing energetics of the free and bound layers leads to the partial formation of a quasi-domain structure in the latter with a lower net magnetization. Whereas both the wetting and free layer magnetizations point in the field direction, the magnetization of the intermediate bound layers orients antiparallel as a result of dipolar interactions. The region between the wetting and free layers actually breaks into two layers in high field, and the fixed particles in the slab closest to the wetting layer experience a frustration as both adjacent-layer magnetizations point in different orientations. The resulting magnetization in this layer is subsequently reduced possibly due to the formation of an in-plane quasi-domain structure triggered by dipolar coupling.

We have thus demonstrated that the interactions between a FF and a solid interface lead to the formation of self-assembled, multilayer structures. The hybrid organic layer that forms on the substrate surface appears to stabilize the complex wetting layer. The composition and thickness of the individual layers that form are sensitive to the competing energetic interactions among the bound, free, and chained NPs in the system. Application of a magnetic field leads to subtle variations in the layer characteristics, whereas free rotation via Brownian motion in more loosely packed regions and Néel relaxation in close-packed configurations give rise to a distinct magnetization behavior and possible quasi-domain formation in the more densely packed layers. Our study thus reveals that both Néel relaxation and Brownian motion have to be taken into consideration to explain the complex structure and magnetic

DOI: 10.1021/acsami.7b14849
ACS Appl. Mater. Interfaces 2018, 10, 5050−5060

behavior of the composite NP stack. These results thus provide a path forward for controlling and tuning these self-assembled structures for device applications.

METHODS

Preparation of NP Ensembles and Si Wafer. The approach used for the synthesis of NPs is the extended LaMers mechanism in which steady-state growth conditions lead to a uniform rate of particle growth and allow for the reproducibility in the particle size, thus resulting in a very low size distribution.[5] The particles used are nicely spherical and have a small diameter size distribution of only 6%, as derived from a histogram of 1000 NPs of a representative transmission electron microscopy (TEM) image. Furthermore, small-angle X-ray scattering measurements were performed, and the data were modeled using a spherical form factor and assuming a Gaussian size distribution. The results were in agreement with those derived from TEM (details are provided elsewhere[5]). For the neutron reflectivity experiments, approximately 1.5 mL of the FF was loaded into a wet cell, which uses a circular Si(100) crystal (diameter of 76 mm and thickness of 5 mm), with one side polished as a solid interface.[45] During the measurements, the wet cell was oriented vertically to avoid NP sedimentation onto the Si surface due to gravity. The silicon wafer was piranha-etched, and an APTES layer was deposited on the surface prior to the experiment. An APTES layer helps the particles to wet the silicon surface as it provides a strong amine bond between its silane groups and the carboxylic acid in the NP shell. The mechanism for and stability of protein adsorption by a silane layer on silicon surfaces is described in the literature.[46]

Characterization of NPs. *SANS.* The SANS experiments were performed at the NG7 SANS instrument at the NIST Center for Neutron Research (NCNR). The samples were loaded into titanium sample cells with quartz windows with a separation of 2 mm. Three detector settings with sample-detector distances of 1, 4, and 15.3 m were used. In the 1 m configuration, the detector was offset horizontally by 25 cm perpendicular to the beam direction to increase the horizontal q-range, where $q = (4\pi \sin \theta)/\lambda$ and θ is the scattering angle relative to the sample surface. A wavelength of $\lambda = 6$ Å was used for the 1 and 4 m configurations, whereas $\lambda = 8.0$ Å neutrons and refractive neutron lenses were used in the 15.3 m configuration to achieve the lowest possible q. The wavelength spread was $\Delta\lambda/\lambda = 11.5\%$ in all configurations. The data were reduced using the NCNR IGOR Pro macros[47] with correction for scattering of the sample cell, ambient background, and variations in the efficiency of detector pixels. The data were scaled by normalizing to the intensity of the incident beam. The two-dimensional SANS data were converted to one-dimensional $I(q)$ versus q curves by circularly averaging over the whole detector. The reduced SANS data were analyzed using the SasView program.[48] The SLD of the Fe_3O_4 core was held fixed for fits to the data shown in Figure 3 because this parameter is correlated with the volume fraction, which was not precisely known for our NP colloid.

Neutron Reflectivity. The neutron reflectivity measurements were carried out on the reflectometer MAGIK at the NCNR[49] using neutrons with a wavelength of 5.0 Å. The wavelength resolution is 1.5% and the angular resolution varied from 1.4 to 1.3% in the investigated q_z-range (both full width at half-maximum). The collimated neutron beam penetrates the edge of the Si crystal and undergoes reflection at the internal interfaces (see Figure S1). The beam footprint on the sample was 25 mm (fixed). Unpolarized and polarized neutron reflectivity measurements were performed under static conditions with small and large magnetic fields applied with an electromagnet parallel to the sample surface (Figure S2). For the PNR measurements, an Fe/Si supermirror and an Al-coil spin flipper were used to select the spin state of the incident neutron beam either parallel (+) to or antiparallel (−) to the applied field. A second supermirror and flipper assembly was used to analyze the spin state of the scattered beam (+ or −). The beam polarization was measured to be 97%. Beam footprint and polarization efficiency corrections were applied to the raw data. For PNR, the nonspin flip cross-sections, (++) and (−−), are sensitive to the nuclear SLD profile Nb(z), and their difference is related to the magnetic depth profile Np(z) for the projection of the magnetization parallel to the applied field. No features were observed in the spin flip cross-sections, confirming that (within the coherent averaging volume of the neutron beam) all in-plane magnetization components perpendicular to the applied field average to zero. Previous studies have shown the coherence volume on this instrument to be approximately 1 μm transverse to the beam and hundreds of micrometers along the beam direction.[40]

The reflectivity data were background corrected and fit to a theoretical model profile by using a fitting routine with a Parratt formalism.[50] The software package Refl1D[41,51] provided by NCNR, the use of which is described in the literature,[52] uses the super-iterative algorithm. The results from fitting the unpolarized reflectivity (Figure S2 in Supporting Information) were used as input for fitting the PNR, from which we determined both Nb(z) and Np(z). Measurements of the unpolarized reflectivity in 100 mT immediately preceded the PNR measurements in the same field, and it was empirically determined that the sample structure did not change substantially during that time. For PNR fits, we thus allowed only small variations with respect to the results we obtained from the fits to the unpolarized data. When fitting each data set, we determined the optimal number of fitting parameters (and thus the optimal number of layers) using the Bayesian information criteria (BIC); $\mathrm{BIC} = (n = k)\,\chi^2 + k\ln(n)$, where n is the total number of data points for the measurement, k is the total number of fitting parameters, and χ^2 represents the reduced χ^2 statistic of the fit, as detailed in ref 33.

As the magnetic SLDs (Np) of the layers containing the NPs are small and their influence to the reflectivity curve is rather weak, it is not sufficient to just fit the reflectivity curves. In addition, the calculated $\mathrm{SA} = (R^{++} - R^{--})/(R^{++} + R^{--})$ was compared to the measured SA, and this comparison allowed refining of the models by rejecting fits for which the SA did not match between the calculation and the measurement. This approach helps in selecting between fits with similar χ^2-values because the SA is extremely sensitive to the Np values. Note that it is not practical to directly fit the SA itself, however, because it is influenced by both the Np values and the structural properties of the layers.

ASSOCIATED CONTENT

Supporting Information

The Supporting Information is available free of charge on the ACS Publications website at DOI: 10.1021/acsami.7b14849.

Details of neutron reflectivity measurements (scattering geometry, unpolarized neutron reflectivity, bulk SLD values, and model calculations) (PDF)

AUTHOR INFORMATION

Corresponding Author

*E-mail: ktheisbroehl@hs-bremerhaven.de. Phone: +49 471 4823471.

ORCID

Katharina Theis-Bröhl: 0000-0002-9218-5588
Dale L. Huber: 0000-0001-6872-8469
Max Wolff: 0000-0002-7517-8204
Kathryn L. Krycka: 0000-0002-6393-3268

Present Address

[¶]Nano-Science Center, Niels Bohr Institute, University of Copenhagen, DK-2100 Copenhagen Ø, Denmark.

Notes

The authors declare no competing financial interest.

ACKNOWLEDGMENTS

This work was performed, in part, at the Center for Integrated Nanotechnologies, the Office of Science User Facility operated for the U.S. Department of Energy (DOE) Office of Science. Sandia National Laboratories is a multimission laboratory

DOI: 10.1021/acsami.7b14849
ACS Appl. Mater. Interfaces 2018, 10, 5050−5060

managed and operated by National Technology and Engineering Solutions of Sandia, LLC., a wholly owned subsidiary of Honeywell International, Inc., for the U.S. Department of Energy's National Nuclear Security Administration under contract DE-NA-0003525. The authors thank Frank Heinrich, NIST Gaithersburg, for support concerning the use of a NIST wet cell. We also thank Paul Kienzle and Cindi Dennis from NIST for fruitful discussions. Furthermore, we thank Benedict Romboy, University of Applied Sciences Bremerhaven, for helping with fitting the data. We gratefully acknowledge the financial support by the NIST guest researchers program, the internal research program by the University of Applied Sciences Bremerhaven, and the DAAD (874454). This work benefited from the use of the SasView application, originally developed under NSF award DMR-0520547. SasView contains code developed with funding from the European Union's Horizon 2020 Research and Innovation Programme under the SINE2020 project, grant agreement no. 654000.

■ ADDITIONAL NOTES

[a]1 emu/cm^3 = 1000 A/m.

[b]Throughout the manuscript, error bars and uncertainties represent one standard error.

■ REFERENCES

(1) Huber, D. L. Synthesis, Properties, and Applications of Iron Nanoparticles. *Small* **2005**, *1*, 482−501.

(2) Herman, D. A. J.; Ferguson, P.; Cheong, S.; Hermans, I. F.; Ruck, B. J.; Allan, K. M.; Prabakar, S.; Spencer, J. L.; Lendrum, C. D.; Tilley, R. D. Hot-injection Synthesis of Iron/Iron Oxide Core/Shell Nanoparticles for T2 Contrast Enhancement in Magnetic Resonance Imaging. *Chem. Commun.* **2011**, *47*, 9221−9223.

(3) Cheong, S.; Ferguson, P.; Hermans, I. F.; Jameson, G. N. L.; Prabakar, S.; Herman, D. A. J.; Tilley, R. D. Synthesis and Stability of Highly Crystalline and Stable Iron/Iron Oxide Core/Shell Nanoparticles for Biomedical Applications. *ChemPlusChem* **2012**, *77*, 135−140.

(4) Sun, S.; Zeng, H. Size-controlled Synthesis of Magnetite Nanoparticles. *J. Am. Chem. Soc.* **2002**, *124*, 8204−8205.

(5) Vreeland, E. C.; Watt, J.; Schober, G. B.; Hance, B. G.; Austin, M. J.; Price, A. D.; Fellows, B. D.; Monson, T. C.; Hudak, N. S.; Maldonado-Camargo, L.; Bohorquez, A. C.; Rinaldi, C.; Huber, D. L. Enhanced Nanoparticle Size Control by Extending LaMers Mechanism. *Chem. Mater.* **2015**, *27*, 6059−6066.

(6) Nie, Z.; Petukhova, A.; Kumacheva, E. Properties and Emerging Applications of Self-assembled Structures Made from Inorganic Nanoparticles. *Nat. Nanotechnol.* **2010**, *5*, 15−25.

(7) Shipway, A. N.; Willner, I. Nanoparticles as Structural and Functional Units in Surface-confined Architectures. *Chem. Commun.* **2001**, *20*, 2035−2045.

(8) Shipway, A. N.; Katz, E.; Willner, I. Nanoparticle Arrays on Surfaces for Electronic, Optical, and Sensor Applications. *ChemPhysChem* **2001**, *1*, 18−52.

(9) Shi, W.; Liang, R.; Xu, S.; Wang, Y.; Luo, C.; Darwish, M.; Smoukov, S. K. Layer-by-Layer Self-Assembly: Toward Magnetic Films with Tunable Anisotropy. *J. Phys. Chem. C* **2015**, *119*, 13215−13223.

(10) Xue, X.; Furlani, E. P. Analysis of the Dynamics of Magnetic Core−Shell Nanoparticles and Self-Assembly of Crystalline Superstructures in Gradient Fields. *J. Phys. Chem. C* **2015**, *119*, 5714−5726.

(11) Xue, X.; Wang, J.; Furlani, E. P. Self-Assembly of Crystalline Structures of Magnetic Core-Shell Nanoparticles for Fabrication of Nanostructured Materials. *ACS Appl. Mater. Interfaces* **2015**, *7*, 22515−22524.

(12) Yethiraj, A.; Thijssen, J. H. J.; Wouterse, A.; van Blaaderen, A. Large Area Electric Field Induced Colloidal Single Crystals for Photonic Applications. *Adv. Mater.* **2004**, *16*, 596−600.

(13) Adolphi, N. L.; Huber, D. L.; Jaetao, J. E.; Bryant, H. C.; Lovato, D. M.; Fegan, D. L.; Venturini, E. L.; Monson, T. C.; Tessier, T. E.; Hathaway, H. J.; Bergemann, C.; Larson, R. S.; Flynn, E. R. Characterization of Magnetite Nanoparticles for SQUID-Relaxometry and Magnetic Needle Biopsy. *J. Magn. Magn. Mater.* **2009**, *321*, 1459−1464.

(14) Adolphi, N. L.; Butler, K. S.; Lovato, D. M.; Tessier, T. E.; Trujillo, J. E.; Hathaway, H. J.; Fegan, D. L.; Monson, T. C.; Stevens, T. E.; Huber, D. L.; Ramu, J.; Milne, M. L.; Altobelli, S. A.; Bryant, H. C.; Larson, R. S.; Flynn, E. R. Imaging of Her2-Targeted Magnetic Nanoparticles for Breast Cancer Detection: Comparison of SQUID Detected Magnetic Relaxometry and MRI. *Contrast Media Mol. Imaging* **2012**, *7*, 308−319.

(15) De Haro, L. P.; Karaulanov, T.; Vreeland, E. C.; Anderson, B.; Hathaway, H. J.; Huber, D. L.; Matlashov, A. N.; Nettles, C. P.; Price, A. D.; Monson, T. C.; Flynn, E. R. Magnetic Relaxometry as Applied to Sensitive Cancer Detection and Localization. *Biomed. Eng.* **2015**, *60*, 445−455.

(16) Khandhar, A. P.; Ferguson, R. M.; Arami, H.; Krishnan, K. M. Monodisperse Magnetite Nanoparticle Tracers for in vivo Magnetic Particle Imaging. *Biomaterials* **2013**, *34*, 3837−3845.

(17) Arami, H.; Krishnan, K. M. Highly Stable Amine Functionalized Iron Oxide Nanoparticles Designed for Magnetic Particle Imaging (MPI). *IEEE Trans. Magn.* **2013**, *49*, 3500−3503.

(18) Xiao, L.; Li, J.; Brougham, D. F.; Fox, E. K.; Feliu, N.; Bushmelev, A.; Schmidt, A.; Mertens, N.; Kiessling, F.; Valldor, M.; Fadeel, B.; Mathur, S. Water-Soluble Superparamagnetic Magnetite Nanoparticles with Biocompatible Coating for Enhanced Magnetic Resonance Imaging. *ACS Nano* **2011**, *5*, 6315−6324.

(19) Deatsch, A. E.; Evans, B. A. Heating Efficiency in Magnetic Nanoparticle Hyperthermia. *J. Magn. Magn. Mater.* **2014**, *354*, 163−172.

(20) Giordano, M. A.; Gutierrez, G.; Rinaldi, C. Fundamental Solutions to the Bioheat Equation and Their Application to Magnetic Fluid Hyperthermia. *Int. J. Hyperthermia* **2010**, *26*, 475−484.

(21) Grzelczak, M.; Vermant, J.; Furst, E. M.; Liz-Marzán, L. M. Directed Self-assembly of Nanoparticles. *ACS Nano* **2010**, *4*, 3591−3605.

(22) Whitesides, G. M.; Grzybowski, B. Self-assembly at All Scales. *Science* **2002**, *295*, 2418−2421.

(23) Ozin, G. A.; Hou, K.; Lotsch, B. V.; Cademartiri, L.; Puzzo, D. P.; Scotognella, F.; Ghadimi, A.; Thomson, J. Nanofabrication by Self-assembly. *Mater. Today* **2009**, *12*, 12−23.

(24) Faraudo, J.; Andreu, J. S.; Calero, C.; Camacho, J. Predicting the Self-Assembly of Superparamagnetic Colloids under Magnetic Fields. *Adv. Funct. Mater.* **2016**, *26*, 3837−3858.

(25) Varòn, M.; Beleggia, M.; Kasama, T.; Harrison, R. J.; Dunin-Borkowski, R. E.; Puntes, V. F.; Frandsen, C. Dipolar Magnetism in Ordered and Disordered Low-dimensional Nanoparticle Assemblies. *Sci. Rep.* **2013**, *3*, 1234.

(26) Wei, A.; Kasama, T.; Dunin-Borkowski, R. E. Self-assembly and Flux Closure Studies of Magnetic Nanoparticle Rings. *J. Mater. Chem.* **2011**, *21*, 16686−16693.

(27) Butter, K.; Bomans, P. H. H.; Frederik, P. M.; Vroege, G. J.; Philipse, A. P. Direct Observation of Dipolar Chains in Iron Ferrofluids by Cryogenic Electron Microscopy. *Nat. Mater.* **2003**, *2*, 88−91.

(28) Elkady, A. S.; Iskakova, L.; Zubarev, A. On the Self-assembly of Net-like Nanostructures in Ferrofluids. *Phys. A* **2015**, *428*, 257−265.

(29) Klokkenburg, M.; Vonk, C.; Claesson, E. M.; Meeldijk, J. D.; Erné, B. H.; Philipse, A. P. Direct Imaging of Zero-field Dipolar Structures in Colloidal Dispersions of Synthetic Magnetite. *J. Am. Chem. Soc.* **2004**, *126*, 16706−16707.

(30) Klokkenburg, M.; Erné, B. H.; Meeldijk, J. D.; Wiedenmann, A.; Petukhov, A. V.; Dullens, R. P. A.; Philipse, A. P. In situ Imaging of Field-induced Hexagonal Columns in Magnetite Ferrofluids. *Phys. Rev. Lett.* **2006**, *97*, 185702.

(31) Puntes, V. F.; Gorostiza, P.; Aruguete, D. M.; Bastus, N. G.; Alivisatos, A. P. Collective Behaviour in Two-dimensional Cobalt

DOI: 10.1021/acsami.7b14849
ACS Appl. Mater. Interfaces 2018, 10, 5050−5060

Nanoparticle Assemblies Observed by Magnetic Force Microscopy. *Nat. Mater.* **2004**, *3*, 263−268.
(32) Krycka, K. L.; Jackson, A. J.; Borchers, J. A.; Shih, J.; Briber, R.; Ivkov, R.; Grüttner, C.; Dennis, C. L. Internal Magnetic Structure of Dextran Coated Magnetite Nanoparticles in Solution Using Small Angle Neutron Scattering with Polarization Analysis. *J. Appl. Phys.* **2011**, *109*, 07B513.
(33) Theis-Bröhl, K.; Gutfreund, P.; Vorobiev, A.; Wolff, M.; Toperverg, B. P.; Dura, J. A.; Borchers, J. A. Self Assembly of Magnetic Nanoparticles at Silicon Surfaces. *Soft Matter* **2015**, *11*, 4695−4704.
(34) Shull, C. G.; Wollan, E. O.; Koehler, W. C. Neutron Scattering and Polarization by Ferromagnetic Materials. *Phys. Rev.* **1951**, *84*, 912.
(35) Hamilton, W. C. Neutron Diffraction Investigation of the 119 K Transition in Magnetite. *Phys. Rev.* **1958**, *110*, 1050−1057.
(36) Standley, K. J. *Oxide Magnetic Materials*; Oxford University, London, 1972; p 23 ff.
(37) Brok, E.; Krycka, E. V.; Gomez, A.; Huber, D. L.; Majkrzak, C. F. Phase-Sensitive Small-Angle Neutron Scattering experiment. *J. Appl. Crystallogr.* **2017**.
(38) Toperverg, B. *Polarized Neutron Scattering*; Brückel, T., Schweika, W., Eds.; Series Matter and Materials; Schriften des Forschungszentrums: Jülich, 2002; Vol. *12*, p 249.
(39) Zabel, H.; Theis Bröhl, K.; Toperverg, B. P. *Handbook of Magnetism and Advanced Magnetic Materials*; Kronmüller, H., Parkin, S., Eds.; Wiley, 2007; p 1237.
(40) Majkrzak, C. F.; Metting, C.; Maranville, B. B.; Dura, J. A.; Satija, S.; Udovic, T.; Berk, N. F. Determination of the Effective Transverse Coherence of the Neutron Wave Packet as Employed in Reflectivity Investigations of Condensed-matter Structures. I. Measurements. *Phys. Rev. A: At., Mol., Opt. Phys.* **2014**, *89*, 033851.
(41) Dura, J. A.; Rus, E. D.; Kienzle, P. A.; Maranville, B. B. *Nanolayer Research: Methodology and Technology for Green Chemistry*; Imae, T., Ed.; Nanolayer Analysis by Neutron Reflectometry; Elsevier, 2017; Vol. *12*, Chapter 5, pp 155−202.
(42) Coffey, W. T.; Kalmykov, Y. P. Thermal Fluctuations of Magnetic Nanoparticles: Fifty Years after Brown. *J. Appl. Phys.* **2012**, *112*, 121301.
(43) Torres-Díaz, I.; Rinaldi, C. Recent Progress in Ferrofluids Research: Novel Applications of Magnetically Controllable and Tunable Fluids. *Soft Matter* **2014**, *10*, 8584−8602.
(44) Mishra, D.; Petracic, O.; Devishvili, A.; Theis-Bröhl, K.; Toperverg, B. P.; Zabel, H. Polarized Neutron Reflectivity from Monolayers of Self-assembled Magnetic Nanoparticles. *J. Phys.: Condens. Matter* **2015**, *27*, 136001.
(45) Kirby, B. J.; Kienzle, P. A.; Maranville, B. B.; Berk, N. F.; Krycka, J.; Heinrich, F.; Majkrzak, C. F. Phase-sensitive Specular Neutron Reflectometry for Imaging the Nanometer Scale Composition Depth Profile of Thin-film Materials. *Curr. Opin. Colloid Interface Sci.* **2012**, *17*, 44−53.
(46) Aissaoui, N.; Bergaoui, L.; Landoulsi, J.; Lambert, J.-F.; Boujday, S. Silane Layers on Silicon Surfaces: Mechanism of Interaction, Stability, and Influence on Protein Adsorption. *Langmuir* **2012**, *28*, 656−665.
(47) Kline, S. R. Reduction and Analysis of SANS and USANS Data Using IGOR Pro. *J. Appl. Crystallogr.* **2006**, *39*, 895−900.
(48) Home page of the Sasview project, retrieved December 12, 2017 from the World Wide Web. http://www.sasview.org/.
(49) Dura, J. A.; Pierce, D. J.; Majkrzak, C. F.; Maliszewskyj, N. C.; McGillivray, D. J.; Lösche, M.; O'Donovan, K. V.; Mihailescu, M.; Perez-Salas, U.; Worcester, D. L.; White, S. H. Advanced Neutron Diffractometer/Reflectometer for Investigation of Thin Films and Multilayers for the Life Sciences. *Rev. Sci. Instrum.* **2006**, *77*, 074301.
(50) Parratt, L. G. Surface Studies of Solids by Total Reflection of X-Rays. *Phys. Rev.* **1954**, *95*, 359.
(51) Kienzle, P.; Maranville, B.; O'Donovan, K.; Ankner, J.; Berk, N.; Majkrzak, C. retrieved December 12, 2017 from the World Wide Web. https://www.nist.gov/ncnr/reflectometry-software.
(52) Owejan, J. E.; Owejan, J. P.; DeCaluwe, S. C.; Dura, J. A. Solid Electrolyte Interphase in Li-Ion Batteries: Evolving Structures Measured In situ by Neutron Reflectometry. *Chem. Mater.* **2012**, *24*, 2133−2140.

DOI: 10.1021/acsami.7b14849
ACS Appl. Mater. Interfaces 2018, 10, 5050−5060